

Article

Improved Detection of Multiple Faint Streak-like Space Targets from a Single Star Image

Yong Han ^{1,2,3,*} , Desheng Wen ¹, Jie Li ² and Zhangchi Qiao ^{1,3}

¹ Xi'an Institute of Optics and Precision Mechanics of CAS, Xi'an 710119, China; ven@opt.ac.cn (D.W.); qiaozhangchi@opt.cn (Z.Q.)

² Department of Information and Communication Engineering, School of Electronic and Information Engineering, Xi'an Jiaotong University, Xi'an 710049, China; jielixjtu@xjtu.edu.cn

³ University of Chinese Academy of Sciences, Beijing 100049, China

* Correspondence: hanyong@opt.cn

Abstract: With the increasing number of human space activities, space surveillance systems need to be developed to reduce the risk of collisions between space assets and space debris. In this context, optical surveillance systems have gradually become a significant means of space surveillance due to their various advantages. Generally, the sidereal tracking mode is used to search for unknown moving targets, which appear as streaks in the star image generated by the optical surveillance system. Typical matched filtering can detect faint streak-like targets in star images, but it generates more false alarms and must traverse all potential filters. In this paper, the layering approach is used to improve the environment for detecting faint targets, in which dual-threshold segmentation is proposed to separate bright objects while maintaining the completeness of faint targets. Second, a streak-like matched filter unit and a dual-step search approach are recommended to lower the computational cost of matched filtering. Finally, perpendicular cross filtering is provided to further eliminate false positives. Experiments performed with both simulated and real data demonstrate that the proposed method has excellent detection performance for detecting multiple faint streak-like targets in a single star image.

Keywords: star image processing; multiple space targets; faint target detection



Academic Editor: Carmine Serio

Received: 17 December 2024

Revised: 5 February 2025

Accepted: 11 February 2025

Published: 12 February 2025

Citation: Han, Y.; Wen, D.; Li, J.; Qiao, Z. Improved Detection of Multiple Faint Streak-like Space Targets from a Single Star Image. *Remote Sens.* **2025**, *17*, 631.

<https://doi.org/10.3390/rs17040631>

Copyright: © 2025 by the authors. Licensee MDPI, Basel, Switzerland. This article is an open access article distributed under the terms and conditions of the Creative Commons Attribution (CC BY) license (<https://creativecommons.org/licenses/by/4.0/>).

1. Introduction

The increasing number of human space activities not only increases the space assets in Earth's orbit year by year but also inevitably brings more space debris, increasingly deteriorating the space environment [1,2]. The need for safe and sustainable space activities requires the development of strong space situation awareness capabilities in an increasingly crowded space environment [3,4]. The space surveillance system, as an important component of space situational awareness, can detect and track space targets. The optical surveillance system is a significant means of space surveillance due to its advantages of low energy consumption, light weight, high reliability, and long-distance observation [5,6]. The star images generated by optical surveillance systems are composed of stars, targets, background, and noise. Stars and targets appear as points or streaks due to their great distance. The background presents a great deal of low-intensity information. Noise is produced by space stray radiation and detection devices, which lowers image quality [7,8]. The sidereal tracking mode (STM) is an important operational mode for space target observation. STM is continuously reoriented to be fixed to the stars, which are stationary and appear as point-like objects. There is relative motion between the optical observation

system and the targets, which appear as streak-like objects [9–11]. As most unknown targets lack knowledge about their orbital parameters, STM is better suited to detect unknown targets [12,13]. In STM, the movement of the target disperses the energy more, making the streak-like target fainter [14,15]. While automatically detecting faint streak-like targets from optical star images is a challenge, better faint streak-like target detection can better detect fainter space targets or allow for the use of lower-cost detectors [16,17].

In recent decades, many methods have been developed to detect streak-like targets from star images, which can be classified into two categories: multi-frame detection and single-frame detection. Multi-frame detection signifies that each detection requires the analysis of successive star images containing the same streak-like targets, and the performance of some approaches may be dependent on the number of successive star images. Leu et al. [18] proposed a segmentation-based approach for detecting space objects in star image sequences through comparing the differences between two successive images. Then, two sets of moving objects are examined in three successive images to identify potential targets. Schildknecht et al. [19] proposed that a mask produced from star image sequences is applied to the star image to be processed, followed by segmentation to detect moving targets. These methods cannot improve the signal-to-noise ratio (SNR) of the targets, so they do not work well for detecting faint targets. The Space-Based Visible (SBV) sensor [20] on the Midcourse Space Experiment (MSX) satellite performs Moving Target Indicator (MTI) algorithms and a 2D velocity-matched filter search to detect streak-like targets. Gural et al. [21] proposed shifting and stacking frames based on a supposed motion speed and direction, then thresholding the multi-frame sum in space and time to identify targets that match the supposed motion. Similarly, Yanagisawa et al. [22] presented a complicated shift-and-co-add method. Various shift values for targets must be applied to ensure that targets are located on the same pixels in subimages, after which field stars are removed and background noise is reduced by the median filter. Danescu et al. [23] proposed a method based on the characteristic that streak-like targets tend to have a collinear trajectory in successive frames. Zhang et al. [24] presented a method based on the movement characteristics to extract and correlate targets from consecutive frames in celestial coordinates. These approaches are mainly based on evaluating each potential motion that could occur in star images. There are also many other multi-frame detection approaches that significantly improve the SNR of moving targets, but the related computing load will rapidly increase as the supposed set grows due to the unknown position, speed, and direction of targets. Furthermore, the image-processing steps in multi-frame detection involve storing a large number of intermediate imagery products that require significant amounts of computer resources. In addition, there may be image shift and rotation, as well as considerable changes in the brightness of the same target between two successive star images. These changes may challenge these approaches based on star image sequences.

Single-frame detection signifies that streak-like targets can be detected in a single image. Stoveken et al. [25] proposed using a star catalog to classify pixels segmented from star images. The pixels corresponding to the star catalog are removed, and the remaining pixels are identified as belonging to targets. Kouprianov et al. [26] presented a logical filtering method based on the bit mask to join these fragments generated by segmentation together. Li et al. [27] developed an approach based on target characteristics. Its operator is used to find local maximum points in each potential target segmented from the star image, and pixels in the same potential target are grouped according to three domains—space, intensity, and distribution—to identify whether it contains a streak-like target. However, these approaches based on segmentation and then classification are better suited for detecting brighter targets. Integrating spatial distribution energy to improve the response intensity of streak-like targets is an effective approach for detecting faint targets.

Yanagisawa et al. [28] developed the line detection method, which assumed the line's direction and integrated the pixel intensity along this direction to enhance the response of a faint target. Zimmer et al. [29] employed the typical Radon transform to identify linear features in star images. The key idea is that faint target detection is equivalent to detecting the local maximum value in the Radon transform domain. Hickson et al. [30] provided a method that combines one-dimensional projection with a fast discrete Radon transform; it projects the image along the perpendicular direction to the track and searches for a local maximum based on the point spread function (PSF) in this one-dimensional projection. These approaches essentially integrate energy along the line distribution, but the length of the line must be sufficiently long. Therefore, it cannot work well for short streak-like targets. Ciurte et al. [31] proposed a method to detect short streak-like targets using the Radon transform in smaller windows, which are then recombined to provide potential targets. A set of additional rules would next be used to determine whether the potential targets are the real targets. Tagawa et al. [32] improved the detection of streak-like targets by compressing images along target directions. The compressed image will have the highest responses if the compression angle and width match the target direction and length, respectively. Nir et al. [33] also present an efficient implementation of the fast Radon transform, which is extended to detect short targets and multiple targets. However, these approaches also require the faint targets to have adequate lengths in order to be detected. At the same time, these methods assume that any residual sources in the image have been eliminated; otherwise, they will result in incorrect results.

Another single-frame detection strategy is the well-known spatial matched filtering, which can integrate all the distributed energy of streak-like targets to improve detection sensitivity in a single image. The idea is that the filter that best matches the streak-like target should give the highest convolution answer. Levesque et al. [34] developed a spatially matched filtering approach to detect known streak-like targets. The streak-like targets should remain after several iterations of matched filtering, while additional residual objects would be attenuated in each iteration of matched filtering. For faint streak-like targets, the detection's performance is limited by false alarms. A method improved by false alarm rejection has been presented [35], in which the length, orientation, and intensity of streak-like target features are used to distinguish between targets and false alarms, and the false alarms can be eliminated further. However, these approaches rely on prior knowledge of the targets, which cannot be obtained in advance for unknown targets. Vananti et al. [36,37] presented a method to detect unknown streak-like targets via spatially matched filtering. Filters of various lengths and directions are generated to convolute a star image, and an overall threshold can be set to accept or reject the responses. To avoid excessive answers caused by filters partially covering streaks or remaining stars, a set of additional accepted criteria has been developed to be used in this method. However, this approach generates a huge number of streak-like filters with various directions and lengths to match the targets, which is time-consuming and computationally intensive. In addition, with the rapid development of machine learning and deep learning, they have also achieved notable results in target detection. Guo et al. [38] introduced a CSAU-Net network for real-time target detection and segmentation based on spatial image features. Zhao et al. [39] developed a deep learning neural network based on the YOLOv5 model to detect and extract targets. Guo et al. [40] also presented a method based on YOLOv8 that can reduce the model parameters while enhancing the faint target detection accuracy. However, these methods typically require a large number of labeled star images as training data, and their robustness and generality to complex background environments that were not included in the training data are limited.

A spatially matched filter that perfectly matches the shape, length, and orientation of a streak-like target should lead to the best detection sensitivity [37,41]. However, it is also sensitive to residual stars and background noise, which may result in many false positives [34–37,41]. Meanwhile, for implementing spatially matched filtering, a blind search is performed on all possible filter lengths and directions due to unknown targets. These significantly increase decision-making difficulties and computational complexity. A good detection method should have excellent detection sensitivity, high decision accuracy, and a reasonable computational effort. Therefore, this study focuses on optimizing the spatially matched filtering to preserve high sensitivity and reduce computing complexity while minimizing false alarms. The contributions of this study are described in the following:

- (1) A star image is separated into three layers: a saturated layer, a bright layer, and a dark layer. The dark layer, which excludes saturated or bright objects, can provide a better environment for detecting faint targets. Dual-threshold segmentation (DTS), which is proposed to separate the dark layer, can ensure the completeness of faint targets in the dark layer. As a result, DTS can effectively reduce false positives caused by bright objects while retaining target detection accuracy.
- (2) Improved streak-like matched filtering is proposed to lower the high computational complexity of matched filtering by optimizing filters for length and direction. A streak-like matched filter unit based on the imaging characteristics of streak-like targets is presented to reduce the number of filters generated for all possible lengths. Meanwhile, a dual-step search is used to reduce the number of searches for all possible filter directions.
- (3) A perpendicular cross filter (PCF) is proposed to eliminate false positives generated by the residual stars and background noise in the dark layer. The PCF is designed to respond differently to streak-like targets and residuals so it can distinguish between them. Therefore, the PCF can further reduce false alarms in the target detection.

The rest of this paper is organized as follows: Section 2 briefly introduces the characteristics of star images. Section 3 describes the essential principles of the proposed detection methods in detail. Section 4 details the implementation and verification of the proposed methods. Experiments and discussion are presented in Section 5, and conclusions are provided in Section 6.

2. Imaging Characteristics

A star image generated by optical instruments is composed of targets, stars, background, and noise. It can be expressed simply as

$$I(i, j) = T(i, j) + S(i, j) + B(i, j) + N(i, j), \quad (1)$$

where $I(i, j)$ is the total intensity value, and $T(i, j)$ and $S(i, j)$ represent space targets and stars, respectively. In STM, stars appear as point-like objects, while targets appear as streak-like objects and can be regarded as the convolution of a point-like object with linear kernels [27]. $B(i, j)$ refers to the background, which is often non-uniform due to the influences of the ecliptic, stray light, and so on. Noise, $N(i, j)$, is generated by space radiation and optical devices, so it is a combination of several kinds of noise [42]. Hot pixels, flicker noise, and other types of similar noise appear as isolated spike noise. Photon noise, dark current, readout noise, and so on all roughly have Poisson or Gaussian distributions and can be approximated as Gaussian noise.

2.1. Distribution of Point-like Stars

Because the stars are fixed relative to the optical system and have a long distance between them, they are imaged as point sources in an exposure period. PSF approximates the energy distribution of each star on the image sensor using a two-dimensional Gaussian function. The energy distribution can be expressed as

$$S_0(i, j) = \frac{I_0}{2\pi\sigma_{\text{PSF}}^2} \exp\left(-\frac{(i-i_0)^2 + (j-j_0)^2}{2\sigma_{\text{PSF}}^2}\right), \quad (2)$$

where I_0 is the total intensity of a star, which is proportional to the total energy transferred from the star to the sensor and can be calculated using the number of electrons collected during the exposure time. σ_{PSF} is the standard deviation of the Gaussian distribution function, which is determined by the optical system's PSF, and (i_0, j_0) is the center position of the star. When k_{area} represents a single pixel area, the intensity value of the star spread across each pixel can be expressed as

$$S(i, j) = \frac{I_0}{2\pi\sigma_{\text{PSF}}^2} \iint_{k_{\text{area}}} \exp\left(-\frac{(i-i_0)^2 + (j-j_0)^2}{2\sigma_{\text{PSF}}^2}\right) didj. \quad (3)$$

2.2. Distribution of Streak-like Targets

Due to the relative motion between the optical observation system and the targets, the energy is dispersed into several pixels along the direction of motion, generating streaks that extend along the motion. The position of the target presented by $(i_0(t), j_0(t))$, which varies with time, is not fixed. The energy distribution can be expressed as

$$T_0(i, j) = \frac{1}{E} \int_0^E \frac{I_0}{2\pi\sigma_{\text{PSF}}^2} \exp\left(-\frac{(i-i_0(t))^2 + (j-j_0(t))^2}{2\sigma_{\text{PSF}}^2}\right) dt, \quad (4)$$

where E is the exposure time. Similar to point-like stars, the intensity value of the target distributed across each pixel can be expressed as

$$T(i, j) = \frac{1}{E} \frac{I_0}{2\pi\sigma_{\text{PSF}}^2} \iint_{k_{\text{area}}} \left[\int_0^E \frac{I_0}{2\pi\sigma_{\text{PSF}}^2} \exp\left(-\frac{(i-i_0(t))^2 + (j-j_0(t))^2}{2\sigma_{\text{PSF}}^2}\right) dt \right] didj. \quad (5)$$

2.3. Object SNR

The SNR is a useful parameter for evaluating the signal quality and mapping the performance of target detection in star images. Target detection becomes more challenging as the SNR decreases. In star images, the object SNR may have different definitions depending on the application environment. Figure 1a illustrates an ideal SNR for a known real signal (S) and noise (σ). In star images, the intensity of the object is distributed across several pixels under the PSF effect, so the ideal SNR is less used. Figure 1b illustrates a peak SNR, which is the ratio of an object's brightest pixel value to its noise. However, objects with the same peak SNR may have pixels with significantly different intensities around the center pixel. As the peak SNR is only related to the pixel with the highest intensity, it does not take into account the intensity of surrounding pixels. Thus, it cannot effectively reflect the object's overall quality. The average SNR involves multiple pixels of the object. As shown in Figure 1c, the different sizes of the average operators provide different results for the same objects. In this study, the size of the local average operator is uniformly defined as the half-height PSF width as shown in Figure 1d. The σ_{PSF} of the PSF in this study is approximately 1.274, derived from the acquired real star images, and its corresponding half-height PSF width is about 3 pixels.

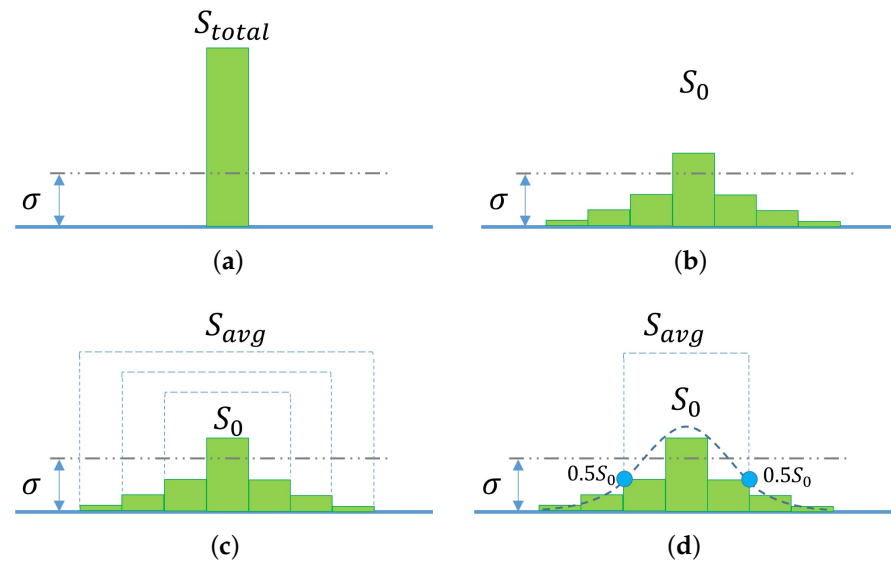


Figure 1. Different definitions of the object's SNR. (a) Ideal SNR; (b) peak SNR; (c) average SNR; (d) average SNR of half-height PSF.

3. Proposed Detection Method

3.1. Image Layering

The saturated region has an adverse impact on star image processing, such as denoising and background estimation, as well as matched filtering. Bright stars or targets can also have an adverse impact on the matched filtering. As shown in Figure 2a,b, bright stars or targets may cause false positives in their surroundings because their energy is strong enough that even partially matched filtering generates higher responses than the perfectly matched filtering of faint streak-like targets. Meanwhile, as shown in Figure 2c, the bright stars around the streak-like target may make it difficult to correctly determine the matched filter's direction. To reduce the negative impact on the detection of faint targets, it is necessary to separate a star image into three layers: a saturated layer, a bright layer, and a dark layer. The saturated layer only includes saturated regions of the star image; the bright layer only includes bright objects of the star image; and the dark layer is the star image after excluding saturated and bright regions. In Figure 2, the gray circular area represents bright stars; the gray streak-like area represents targets; the region surrounded by the blue line represents the filter; and the black dot represents the center of the filter.

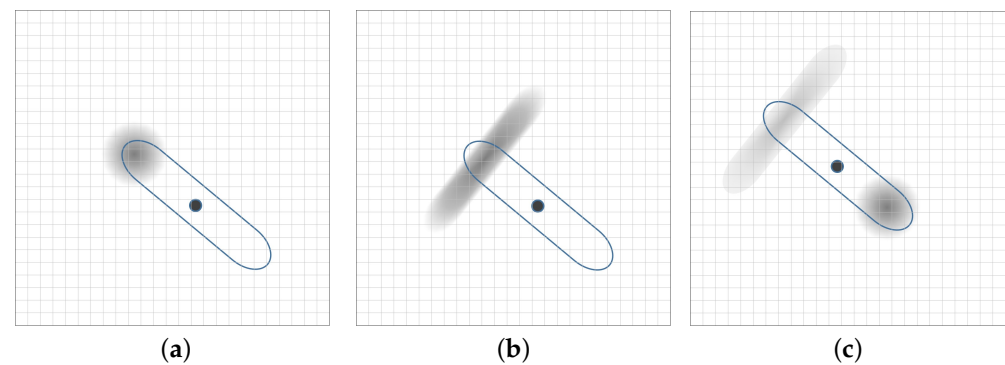


Figure 2. The influence of bright objects on faint target detection based on matched filtering. (a) Bright stars cause false positives in their surroundings. (b) Bright targets cause false positives in their surroundings. (c) Bright stars around the streak-like target generate higher responses in the incorrect direction.

3.1.1. Saturated Region Extraction

A normal star image that can be processed successfully should only have a few or no saturated areas. The saturated layer is separated as follows: Firstly, the saturation intensity threshold (T_{Sat_Mag}) can be estimated according to the star image's grayscale, and then the star image is segmented to obtain saturated pixels. Secondly, the region-growing method is applied to the saturated pixels to obtain each saturated object. If the size of these objects exceeds the size threshold (T_{Sat_Area}), they are classified as saturated objects. Finally, the saturated layer is composed of expanded saturated object regions to avoid leaving residues.

In Figure 3 (left), the gray circular area represents saturated stars, and the gray grid area shows saturated pixels caused by isolated spike noise. Figure 3 (middle) shows the six potential saturated objects that were extracted from the star image by the segmentation and region-growing methods. Object 2 and Object 3 meet the size requirement, so they are classified as saturated objects. Figure 3 (right) shows that the saturated layer consists of Object 2 and Object 3. Object 1 and Object 4 are stars in critical saturation, which means their distribution profiles have not suffered significant damage. Therefore, they will be classified as bright objects and separated into bright layers. Object 5 and Object 6, which do not meet the size requirement, are eliminated as spike noise in the star image preprocessing.

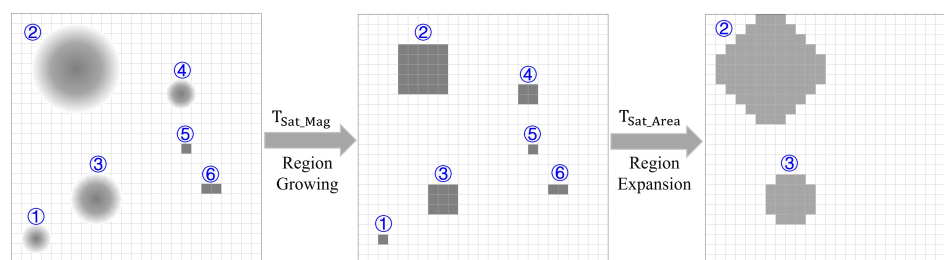


Figure 3. The saturated layer is separated from the star image. **(Left)** Initial saturated star image. **(Middle)** Connecting area of saturated pixels. **(Right)** Saturated objects are separated.

3.1.2. Dual-Threshold Segmentation

After the saturated layer separation, background removal, and denoising, the star image can be separated into bright and dark layers. As the intensity of bright objects is high, they can be segmented directly with traditional threshold segmentation (TTS). However, streak-like targets near the threshold may be broken into one or more discontinuous fragments, resulting in incomplete streak-like targets or the misclassification of some fragments as stars. In Figure 4a, Object 1 is a faint star; Object 2 is a streak-like target near the threshold; Object 3 is a bright star; Object 4 is a bright streak-like target; Object 5 is a star near the threshold; and Object 6 is a faint streak-like target. The results of TTS are shown in Figure 4b. Object 3 and Object 4 can be completely segmented. Object 1 and Object 6 are separated into the dark layer. Object 5 is not segmented, so it is left in the dark layer due to its tiny area. Object 2 is improperly segmented into two new objects: Object 7 and Object 8. Object 7 is difficult to detect as a streak-like target due to the severe damage. Object 8 is likely to be misidentified as a star, resulting in the loss of the observed targets. Therefore, the faint streak-like targets near the threshold may be damaged by TTS.

The basic idea of DTS is that two thresholds, a high threshold and a low threshold, are used to segment the same object, resulting in two areas of different sizes. The ratio between the two areas of the same object, presented as a size-extended ratio, is used to determine which layer it belongs to. For a fainter target, there are no or only very small areas in the results of high-threshold segmentation, so it can be directly separated into the dark layer without considering its results in low-threshold segmentation. For a bright object, the area obtained by low-threshold segmentation is a natural extension of the area

obtained by high-threshold segmentation, so the size-extended ratio is not sharp. For an object near the threshold, the area obtained by low-threshold segmentation includes not only the natural extension of the area obtained by high-threshold segmentation but also its fragments that were not in the results of high-threshold segmentation, so its size-extended ratio is sharp. Therefore, it is possible to determine whether an object belongs to the bright layer or the dark layer by comparing its area in the results of low-threshold segmentation to that of high-threshold segmentation.

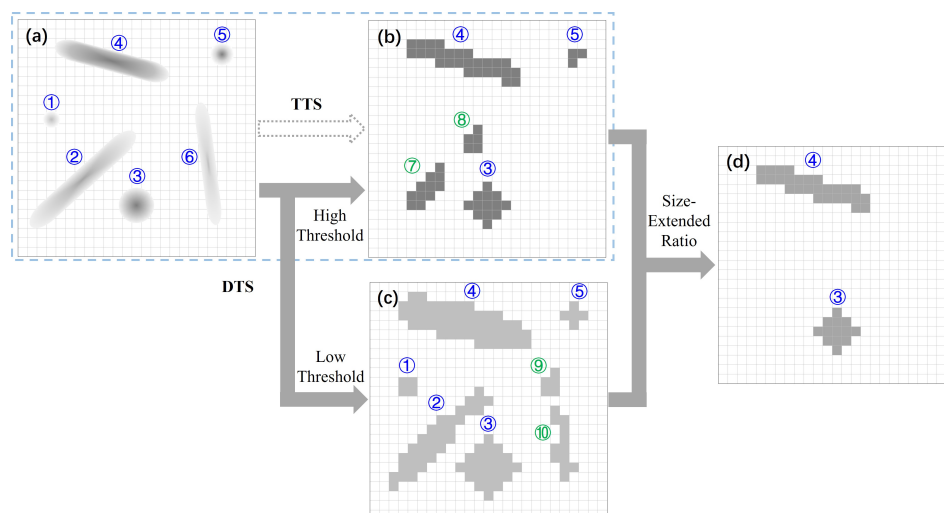


Figure 4. Separate bright and dark layers. (a) Initial star image including multiple objects. (b) Bright objects separated by TTS (objects separated by DTS with the high threshold). (c) Objects separated by DTS with the low threshold. (d) Bright objects separated by DTS.

Figure 4c shows the results of low-threshold segmentation, and Figure 4d shows the DTS results. The areas of Object 3 and Object 4 in the results of low-threshold segmentation are natural outward extensions of their corresponding high-threshold areas, so they can be separated into the bright layer. Object 1 is left in the dark layer because it is not in the results of high-threshold segmentation. Similarly, Object 6 is left in the dark layer. Object 5 is left in the dark layer due to its tiny area in the results of the high-threshold segmentation. Object 2 is broken into two areas by high-threshold segmentation. When they are compared with their corresponding areas by low-threshold segmentation, their size-extended ratios are sharp, so Object 2 is retained in the dark layer. By comparing Figure 4b,d, Object 3 and Object 4 are successfully separated into the bright layer; Object 1, Object 5, and Object 6 are correctly separated into the dark layer by TTS or DTS. Only DTS can separate Object 2 completely into the dark layer, while TTS cannot.

At present, the star image is separated into three layers. Point-like stars and streak-like targets in the bright layer can be identified by their characteristics and structure. After removing the saturated layer and bright layer from the star image, the dark layer is obtained, which only contains faint objects. Thus, the image layering eliminates the influence of saturated and bright objects and protects the completeness of faint streak-like targets, making it better suited for the streak-like target detection of matched filtering.

3.2. Improved Streak-like Matched Filtering

The idea of streak-like matched filtering is that the filter that best matches the streak-like target should produce the highest response. It convolves the star image $I(i, j)$ with all possible streak-like filters $F(l, \theta)$ [37] and compares the response to a threshold η as

$$\frac{\arg \max_{(l,\theta)}(I(i,j) * F(l,\theta))}{\sigma_F} > \eta. \quad (6)$$

σ_F represents the filtered image noise, and it is calculated according to the matched filter [37]. The l represents the streak-like filter's length, and θ represents its direction. Due to the lack of prior information for unknown targets, all possible filters (with variable lengths and angles) must be produced in advance, which can result in significant computational costs in filtering. Therefore, streak-like matched filtering can be improved by decreasing the number of possible filters based on these two factors.

3.2.1. Streak-like Matched Filter Unit

The generation of the streak-like matched filter reveals that the distribution of the filter in the direction of the perpendicular to the filter's orientation is nearly identical, with the exception of both ends of the streak-like filter as shown in Figure 5a,b. A streak-like matched filter can be approximated by combining several streak-like matched filter units. The longer the streak-like matched filter, the higher the detection sensitivity; however, it needs to meet the requirement that there must be a faint target with the same length in the star image. Figure 5c shows the filter results for the streak-like matched filter unit. The filter response obviously increases as the target SNR increases, but it changes slightly with the length of the target. When the target length is nearly the same as the length of the filter unit, the energy at both ends of the target will be lower than that of the longer target. Therefore, there is a drop in the response of the matched filter unit to the 21-pixel-long target. It can be concluded that the detection sensitivity is almost determined by the length of the filter unit and is not related to the length of the target. Therefore, the length of the streak-like matched filter unit can be determined based on the detection sensitivity requirements and the detected target's minimum length. For $\sigma_{PSF} = 1.274$, a 7×7 window contains 99% of the energy of a point-like object. Its three-times width, 21 pixels, is chosen as the minimum detectable length for the streak-like target in this paper. As the streak-like matched filter unit has a defined length, the search for the matched filter is limited to only all possible directions, avoiding the need to search all potential lengths.

3.2.2. Dual-Step Angle Search

The matched filter's direction search is to find the matched direction of the streak-like target within the range of 0° to 180° . Because the filtering response in adjacent directions of the matched direction is also related to the maximum filtering response, a dual-step search can be proposed to simplify the direction-blind search. The first phase is a large-step coarse search to determine a small direction range that includes the matched direction. The second phase is a small-step fine search to find the matched direction within this range. As shown in Figure 6, the gray short dash represents all of the responses to various angles in the large-step coarse search. And the gray dotted line, which is the maximum response, represents the result of the large-step coarse search. Expanding it to both sides results in the small search range. And a small-step fine search in the range is performed to obtain the matched direction represented by the green long dash. The step size of coarse search impacts the validity of direction search, computational complexity, and implementation convenience. The comparison of the response ratio and search times for different large-step sizes with a directional resolution of 1° is shown in Table 1. The response ratio in Table 1 is the ratio of the maximum response of the large-step coarse search to the maximum filtering response of the blind search, and the search times in Table 1 is the number of search times in a dual-step angle search. The lower the response ratio, the worse the relevance. The fewer the search times, the lower the computational cost.

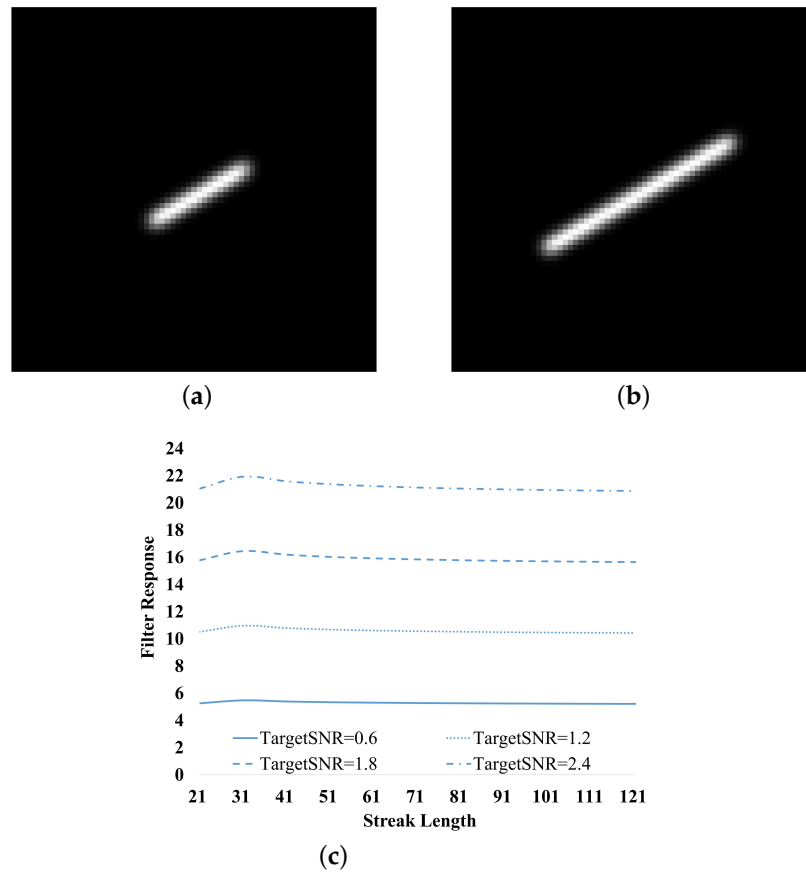


Figure 5. The distribution and filtering response of a streak-like matched filter unit: (a) A streak-like matched filter with a length of 21 pixels. (b) A streak-like matched filter with a length of 41 pixels. (c) The responses of a streak-like matched filter unit of 21-pixel length filtering the same SNR streak-like targets with various lengths.

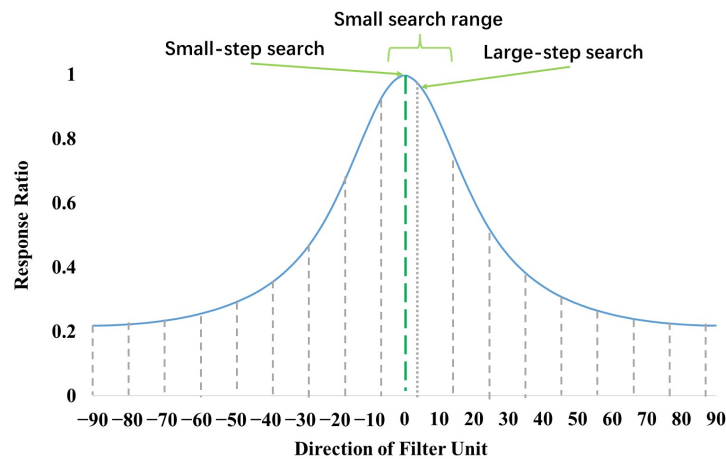


Figure 6. The dual-step search for the matched direction.

Table 1. The response ratios and search times for different large-step sizes.

Step size	1	2	3	4	5	6
Response ratio	100%	99.58%	98.98%	98.19%	97.06%	95.71%
Search times	180	92	64	51	44	40
Step size	9	10	12	15	18	20
Response ratio	90.13%	87.93%	83.09%	75.45%	67.88%	63.19%
Search times	36	36	37	40	44	47

3.3. Perpendicular-Cross Filtering

After layering and matched filtering, faint streak-like targets can be well detected in the dark layer, but the residual faint stars and noise may still cause false positives. In order to further reduce these false positives, PCF based on the differences in response to the perpendicular direction of matched filters between stars and streak-like targets is proposed. The difference in response for a star between the direction of the filter with maximum response (MF_{MAX}) and perpendicular to it (MF_{PC}) is caused by noise, and the difference is limited to a specified range that is related to noise as shown in Figure 7a. The difference in response for a streak-like target between the direction of the matched filter (MF_{MAX}) and perpendicular to it (MF_{PC}) is mainly determined by the structure of the target itself, and the difference will be greater than that of the star as shown in Figure 7b. The response ratio of PCF is defined as

$$R_{PCF} = \frac{MF_{MAX}}{MF_{PC}}. \quad (7)$$

For example, in an ideal environment, for a streak-like matched filter with a length of 21 pixels, the R_{PCF} of stars is roughly 1, while the R_{PCF} of a streak-like target is approximately 4.5. Therefore, the PCF can be used to further eliminate false alarms caused by residual stars and noise, which only requires one additional filtering calculation. In Figure 7, the region enclosed by the solid line represents the matched filter, and θ represents the direction of the matched filter. The region enclosed by the dashed line represents the perpendicular cross filter corresponding to the matched filter, and $\theta-90$ represents the direction of the perpendicular cross filter. The gray areas represent point-like stars and streak-like targets. The black dot represents the center of the filters.

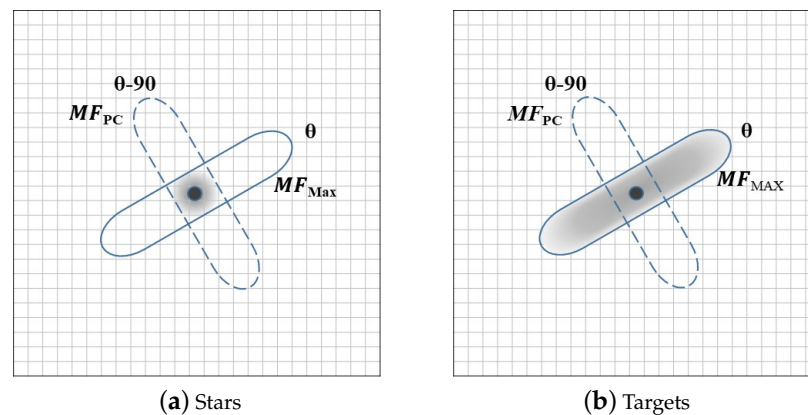


Figure 7. The PCF is used for the stars and the streak-like targets.

4. Implementation and Verification

The entire process of detecting multiple targets in a star image is described as schematically illustrated in Figure 8. The saturated layer is first separated from the raw star image, followed by image preprocessing to remove background and noise. Secondly, the preprocessed image is enhanced, and then DTS is used to separate the bright and dark layers. The typical geometry-based classification method is used to identify bright targets in the bright layers. In the dark layer, the improved streak-like matched filtering is used to identify faint targets, and then PCF is used to further eliminate false alarms. Finally, the detected streak-like targets in a single star image are composed of bright targets and faint targets.

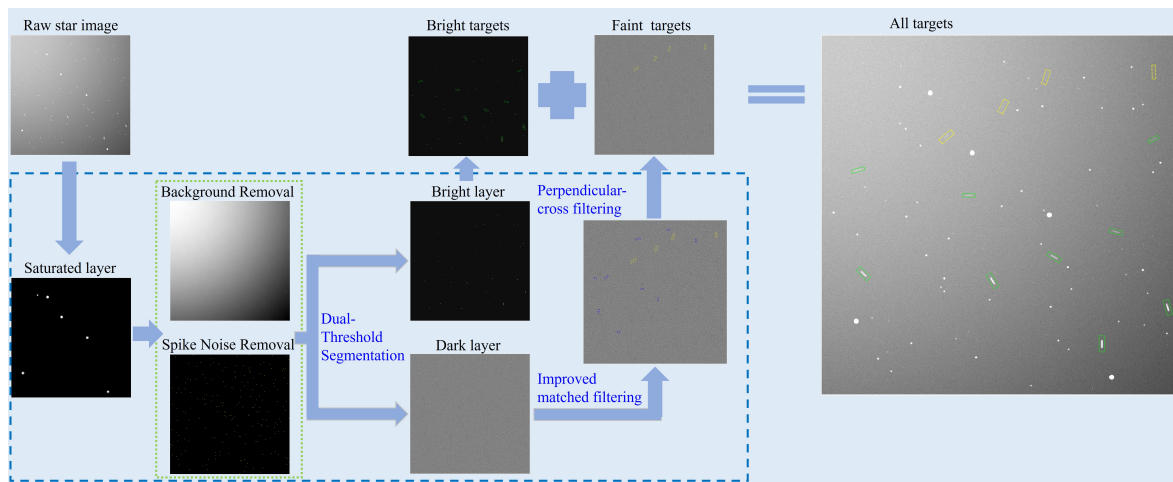


Figure 8. The workflow of detecting multiple targets in a single star image. The targets detected in the bright layer are shown by green-line rectangles. The false positives removed in the dark layer are shown by blue-dash rectangles. The targets detected in the dark layer are shown by yellow-dot rectangles.

4.1. Separation of Saturated Layer

As stated in Section 3.1.1, because the star image's grayscale is 16-bit, the saturation intensity threshold (T_{Sat_Mag}) can be set to 60,000. Additionally, the saturated object area threshold (T_{Sat_Area}) is set to 4 pixels due to the fact that the smaller objects are critically saturated stars or spike noise. As shown in Figure 9, the saturated layer containing six saturated objects is separated from the star image.

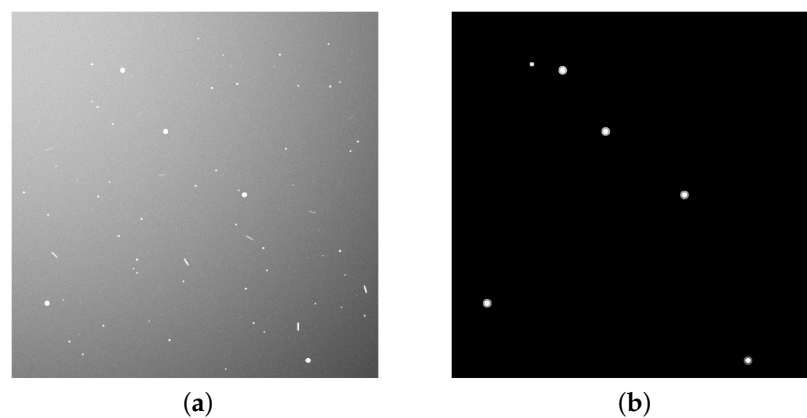


Figure 9. Separating the saturated layer from the raw star image: (a) the raw star image; (b) the saturated layer.

4.2. Star Image Preprocessing

It is required to preprocess the star image to suppress or eliminate the interference of the non-uniform background and noise on target detection. This section details the approaches to background estimation, noise statistics, and spike noise removal. Figure 10c shows the preprocessed star image, which is used as the input for subsequent target detection.

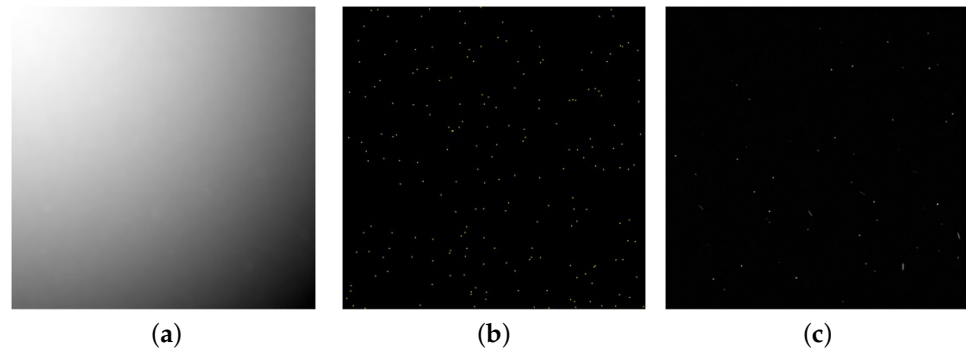


Figure 10. Star image preprocessing: (a) background estimation; (b) spike noise; (c) star image after removing background and spike noise.

4.2.1. Background Estimation

If the background is not properly estimated, it may result in two problems. The first is that a portion of the target signal is removed along with the background, weakening the responses of faint targets and leading to detection failure. Another problem is that the residual background may lead to excessive responses in target detection, resulting in false positives. The median filter is a popular background estimation method. One advantage of the median filter is that it can better keep the initial image's faint object. However, the size of the operator kernel is difficult to determine. If the size is set too small, it will destroy the objects. Alternatively, setting the size too large will raise the computational cost and damage the local feature. After removing the saturated layer, there will be no large-sized interested stars or targets in the star image. The operator kernel size is usually 5~10 times the width of the PSF; thus, a median filter of 15×15 is chosen in this study. Figure 10a shows the background estimation.

4.2.2. Noise Statistics

After the saturated layer and the background have been removed, the presence of bright stars, bright targets, and spike noise in the star image can deteriorate the accuracy of noise statistics. In this study, two iterations of statistics are adopted to counteract these deteriorations in noise statistics. The specific steps are as follows:

- (1) Noise statistics are estimated from the star image $I'(i, j)$, which is the star image after removing the saturated layer and background, and the mean and variance are obtained as

$$\mu_0 = \frac{\sum_{i=1}^M \sum_{j=1}^N I'(i, j)}{N_I} \quad \sigma_0 = \frac{\sqrt{\sum_{i=1}^M \sum_{j=1}^N (I'(i, j) - \mu_0)^2}}{N_I - 1}. \quad (8)$$

- (2) The first segmentation of the star image generates a binary image, such as

$$B(i, j) = \begin{cases} 1 & I'(i, j) > T_{th0} \\ 0 & \text{else} \end{cases} \quad T_{th0} = \mu_0 + k\sigma_0. \quad (9)$$

- (3) The star image containing noise is

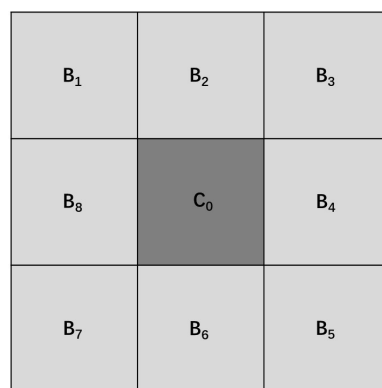
$$\tilde{n}(i, j) = I'(i, j) * (1 - B(i, j)), \quad (10)$$

which is used to calculate the mean and variance of the noise as follows:

$$\mu_n = \frac{\sum_{i=1}^M \sum_{j=1}^N \tilde{n}(i, j)}{N_n} \quad \sigma_n = \frac{\sqrt{\sum_{i=1}^M \sum_{j=1}^N (\tilde{n}(i, j) - \mu_n)^2}}{N_n - 1}. \quad (11)$$

4.2.3. Spike Noise Removal

The spike noise in the star image may be misunderstood as objects; thus, it must be eliminated at this stage. Under the effect of PSF, the object's energy spreads into the surrounding area, and the intensity of the surrounding pixels has a relationship to the center pixel. This relationship does not exist in spike noise. Spike noise is a single pixel with exceptional brightness far above the main distribution, which can be easily identified and removed. Hence, a simple but efficient filter was designed to detect and remove this spike noise. The filter is shown in Figure 11. When a pixel C_0 has an intensity greater than $5\sigma_n$ and its neighboring pixels B_i have intensities less than $3\sigma_n$, the pixel C_0 can be identified as spike noise and should be removed. To be appropriate for continuous spike noise detection, the neighbor's maximum intensity of the requirement is optimized to the neighbor's second maximum intensity. Figure 10b shows the spike noise detection results in a simulated star image containing 200 randomly generated spikes. The average probability of eliminating spike noises in these 100 simulated star images is 99.39%.



If $C_0 > 5\sigma_n$ and $\text{SecondMax}(B_i) < 3\sigma_n : C_0 = 0$
 $i = 1 \dots 8$

Figure 11. Principle of spike noise removal.

4.3. Separation of Bright and Dark Layers

Following the removal of the saturated layer and preprocessing, a typical Gaussian kernel that corresponds to the PSF is utilized to enhance the image for better separating the bright and dark layers. The objects in the bright layer are classified using a typical geometry-based classification method, which examines the lengths of the semi-major and semi-minor axes of the objects. At this stage, bright objects have been classified as streak-like targets, point-like stars, or other objects that fail to meet the requirements of the first two types, and these objects are left in the dark layer for further analysis. As shown in Figure 12, the green rectangle represents the detected streak-like targets; the yellow circle represents the detected stars; and the red-dash square represents the area where the streak object is mistakenly detected as a point-like object by TTS. Figure 12a shows that two faint targets are mistakenly detected as stars, while these two objects are left in the dark layer by DTS without being damaged as shown in Figure 12b. As mentioned in Section 3.1.2, DTS can effectively maintain the completeness of streak-like targets. To evaluate the performance of the proposed method, four metrics are defined as follows:

The star elimination probability is

$$P_{se} = \frac{\text{the number of stars correctly identified}}{\text{the total number of stars}}. \quad (12)$$

The target recognition probability is

$$P_{tr} = \frac{\text{the number of complete targets correctly identified}}{\text{the total number of targets}}. \quad (13)$$

The false alarm probability is

$$P_{fa} = \frac{\text{the number of false targets}}{\text{the total number of stars}}. \quad (14)$$

The target damage probability is

$$P_{td} = \frac{\text{the number of damaged targets that are incomplete or incorrectly identified}}{\text{the total number of targets}}. \quad (15)$$

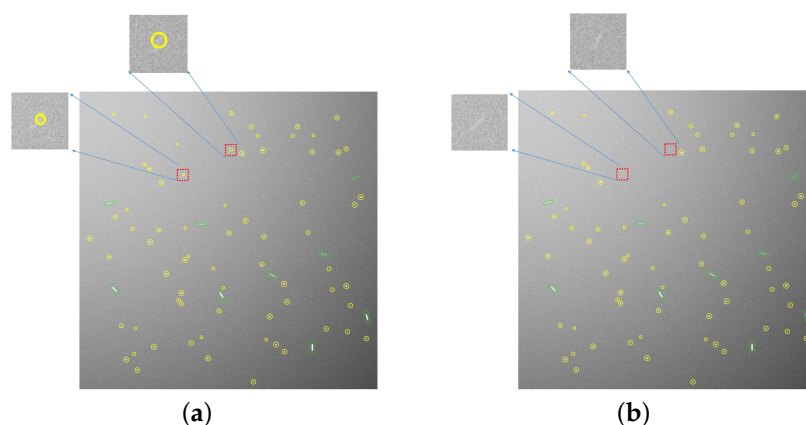


Figure 12. Separate the bright and dark layers: (a) separation of bright and dark layers by TTS; (b) separation of bright and dark layers by DTS.

As shown in Figure 13, DTS has a lower P_{se} than TTS under the same conditions. The stars near the segmentation threshold that are obtained in the results of the high-threshold segmentation but fail to meet the requirement of the size-extended ratio cannot be eliminated by DTS. But they will be further eliminated in the dark layer. It can also be seen that P_{se} is independent of the target SNR and length but is only affected by the star SNR. Figure 13a shows that DTS can eliminate all stars in the bright layer when the star SNR exceeds 3.5. Therefore, DTS can also successfully eliminate stars in the bright layer.

As shown in Figure 14, the P_{tr} of DTS, similar to P_{se} , is lower than that of TTS under the same conditions. But these targets that are not detected by DTS will be further detected in the dark layer. Figure 14a shows that P_{tr} is independent of the star SNR. Figure 14c shows that P_{tr} increases as the target SNR increases. Figure 14b shows that the P_{tr} of targets near the segmentation threshold decreases as the target length increases. This is because targets near the segmentation threshold are more easily segmented into multiple fragments as the length increases. Once the target SNR increases beyond the range around the segmentation threshold, P_{tr} is no longer affected by length. As shown in Figure 14b,c, DTS can detect all targets when the target SNR exceeds 2.8. Therefore, DTS can also successfully recognize targets in the bright layer.

The P_{fa} values of DTS and TTS are nearly zero. The saturated objects are separated in the saturated layer, and the stars and residual noise obtained by DTS or TTS in the bright layer can hardly meet the requirements of the typical geometry-based classification. Therefore, there are almost no false positives in the bright layer.

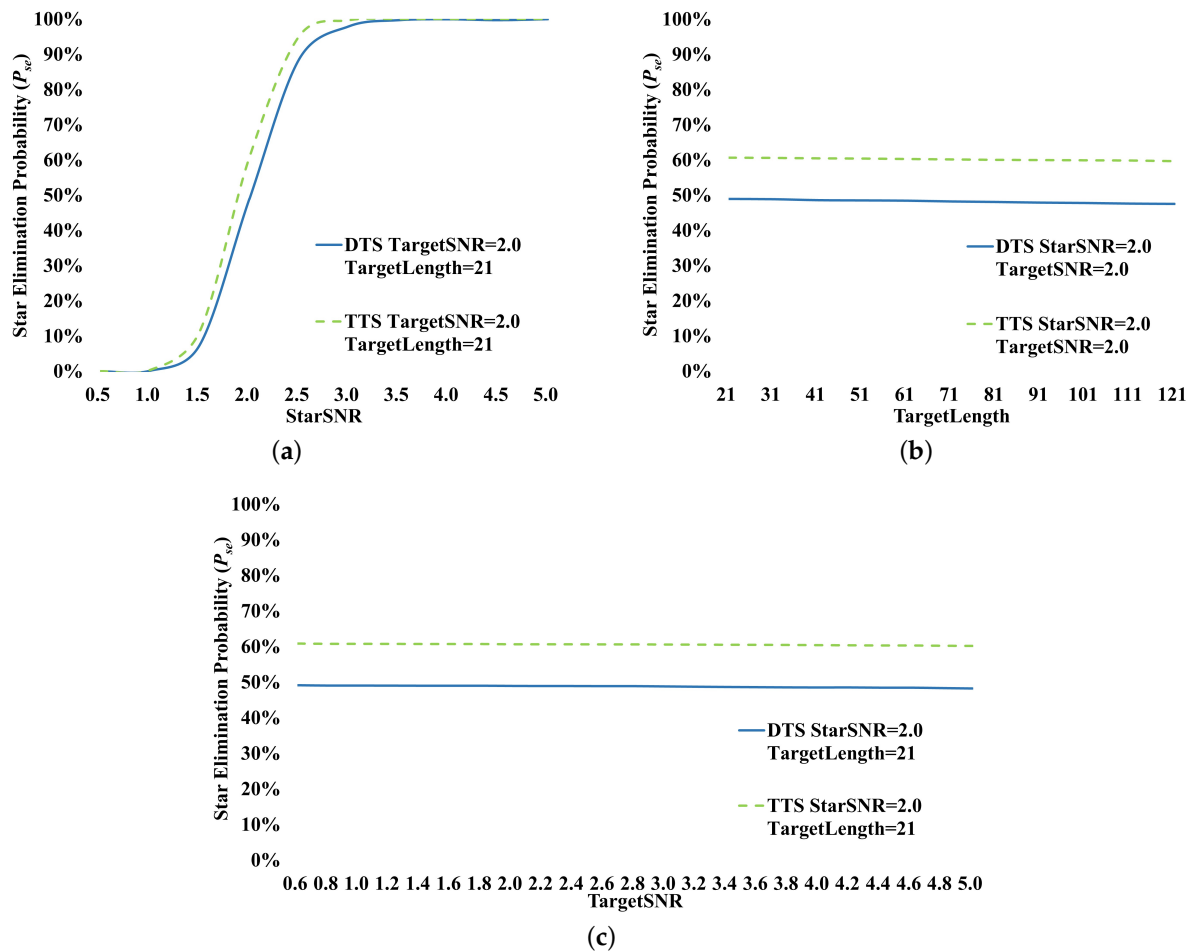


Figure 13. Comparison of P_{se} between TTS and DTS. (a) P_{se} with different star SNR; (b) P_{se} with different target lengths; (c) P_{se} with different target SNR.

Figure 15a shows that P_{td} is independent of the star SNR. Figure 15c shows that TTS can cause significant damage to targets with an SNR ranging from 1.0 to 2.2. This is because these faint targets are segmented into many fragments by TTS under the influence of noise, which can be misidentified as one or more incomplete targets or stars. Figure 15b shows that the P_{td} of TTS grows as the target length increases. This is because faint targets with longer lengths are more likely to be segmented into fragments. As shown in Figure 15, the maximum P_{td} of DTS is less than 1% at various target SNRs and lengths. However, TTS can exceed 90%, which implies that TTS has significant adverse effects on the detection ability of faint targets. Because the fragments of targets obtained by high-threshold segmentation fail to meet the requirement of the size-extended ratio in DTS, they are left completely in the dark layer without being damaged.

In summary, the faint targets near the segmentation threshold may be misidentified as incomplete targets or stars by TTS, while they are almost preserved completely in the dark layer by DTS. DTS not only effectively recognizes bright targets and removes bright stars but also successfully ensures the completeness of faint targets. Therefore, DTS has greater advantages in separating the bright and dark layers.

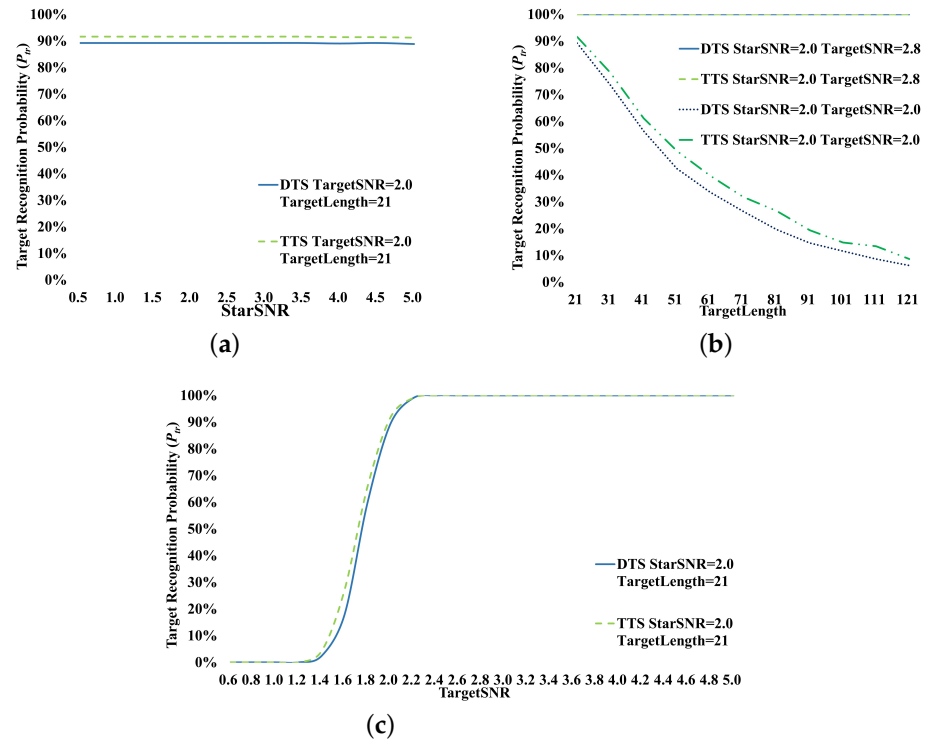


Figure 14. Comparison of P_{tr} between TTS and DTS. (a) P_{tr} with different star SNR; (b) P_{tr} with different target lengths; (c) P_{tr} with different target SNR.

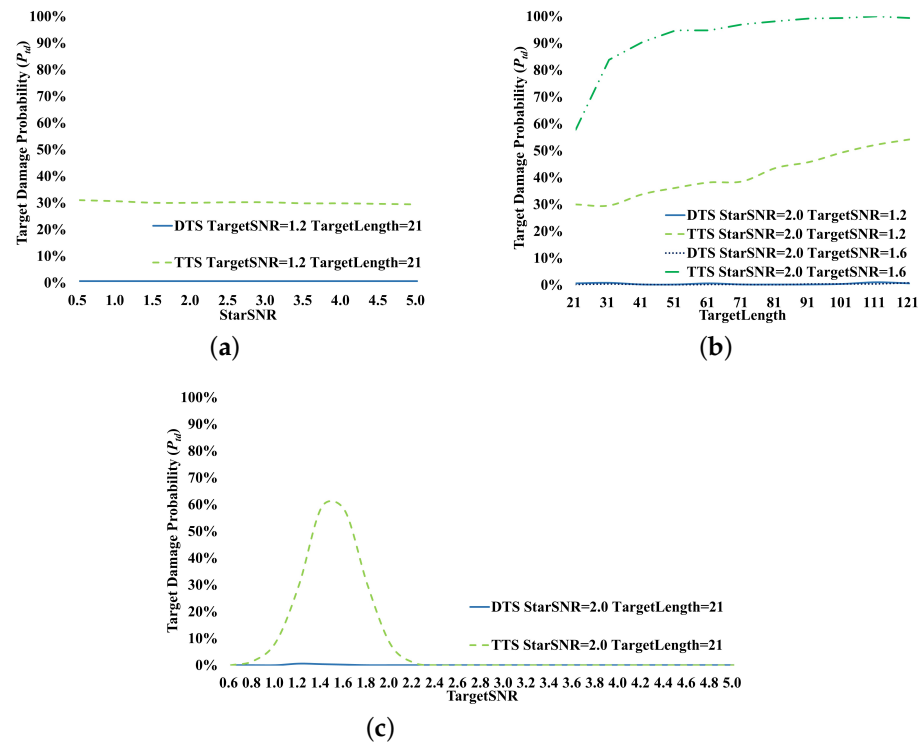


Figure 15. Comparison of P_{id} between TTS and DTS. (a) P_{id} with different star SNR; (b) P_{id} with different target lengths; (c) P_{id} with different target SNR.

4.4. Filtering Response of Faint Streak-like Target

As described in Section 3.2, matched filtering is performed to detect faint streak-like targets in the dark layer based on Equation (6), and all filters should be created in advance according to Equation (5). The improved streak-like matched filter unit is intended to lower

computational costs by reducing the number of filters required for matching. For example, filters are set to a length set $\{L\}$ of 21–121 pixels with a step size of 2 pixels and an angle set $\{\theta\}$ of 1–180° with a step size of 1°. The number of filter iterations for the typical matched filtering is 9180, while that of the improved matched filtering is reduced to 44. According to Section 3.2, the length of the improved streak-like matched filter unit is set to 21 pixels, and the detection sensitivity on this condition will be evaluated in Section 5. When the filter length is determined, the dual-step search in directions can be verified by comparing the filtering responses and the computing time to the typical matched filtering in the object regions. A blind search of the typical matched filters' direction is performed with a resolution of 1°. The large-step sizes of the dual-step search are 2°, 3°, 4°, 5°, 6°, 9°, and 10°, respectively, and the small-step size of the dual-step search is 1°, which is the same resolution as the blind search. The response consistency ratio and the computation cost ratio are defined as follows:

$$R_{rc} = \frac{\text{the number of pixels with the same response between the dual-step search and the blind search}}{\text{the total number of pixels}} \quad (16)$$

$$R_{cc} = \frac{\text{the time of the dual-step search}}{\text{the time of the blind search}}, \quad (17)$$

which are used separately to evaluate the negative impact on filter response and the positive impact on computational cost.

As shown in Figure 16, when the large-step size is set to 2°, the computational cost is higher due to the greater number of searches, and its R_{rc} is also lower than 3°'s R_{rc} . The smaller small-step search range determined by the large-step size can increase the probability that the small-step search range does not include the matched angle, so its R_{rc} is lower. Therefore, the large-step size cannot be set too small. When the large-step size is set to 9° or 10°, the computational cost is lower, but the R_{rc} is very poor. The filtering response of the large-step search is sharply reduced as the large-step size increases, which may result in an incorrect large-scale search result, causing a significant reduction in R_{rc} . Therefore, the large-step size cannot be set too large. In this study, the large-step size is set to 5°, which can help to balance the effect between R_{cc} and R_{rc} . Under this condition, R_{rc} is 99.88% and R_{cc} is 25.17%, indicating that the method has lower computational costs while maintaining the same filtering responses.

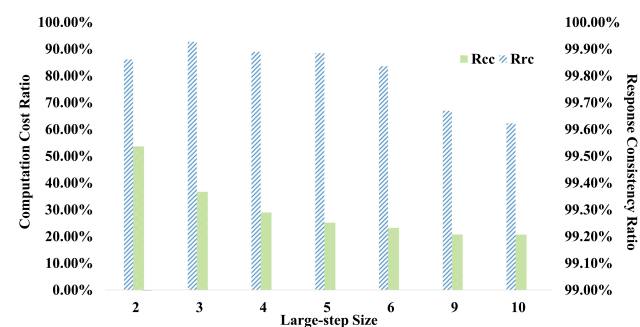


Figure 16. Dual-step search with different large-step sizes for the direction search of streak-like matched filter units.

4.5. False Alarm Removal

The faint targets can be identified by segmenting the matched filtering response, but residual stars and noise can cause some false positives. As mentioned in Section 3.3, the PCF is developed to reduce these false positives, so the impact of the PCF on target

detection performance is necessary to be verified. The removal probability of false alarms and the retention probability of true targets are defined as follows:

$$P_{far} = \frac{\text{the number of false positives removed with PCF}}{\text{the total number of false positives without PCF}} \quad (18)$$

$$P_{ttr} = \frac{\text{the number of targets correctly identified with PCF}}{\text{the number of targets correctly identified without PCF}} \quad (19)$$

As shown in Figure 17a, when the star SNR is less than 1.5, the P_{far} decreases as the star SNR increases; when the star SNR is close to 1.5, it reaches its lowest value. In this situation, most false positives are difficult to meet the requirements of PCF since they are largely dominated by noise rather than faint objects. Therefore, the total number of false positives detected by matched filtering increases rapidly as the star SNR increases, while the number of false positives removed does not increase so rapidly. When the star SNR exceeds 1.5, the number of such false positives that can meet the requirements of PCF begins to rapidly increase since they are largely dominated by the faint objects. Figure 17 shows that when the star's SNR is equal to 1.5, the lowest value of P_{far} can still be greater than 77%. Most of the false positives can be successfully removed by PCF.

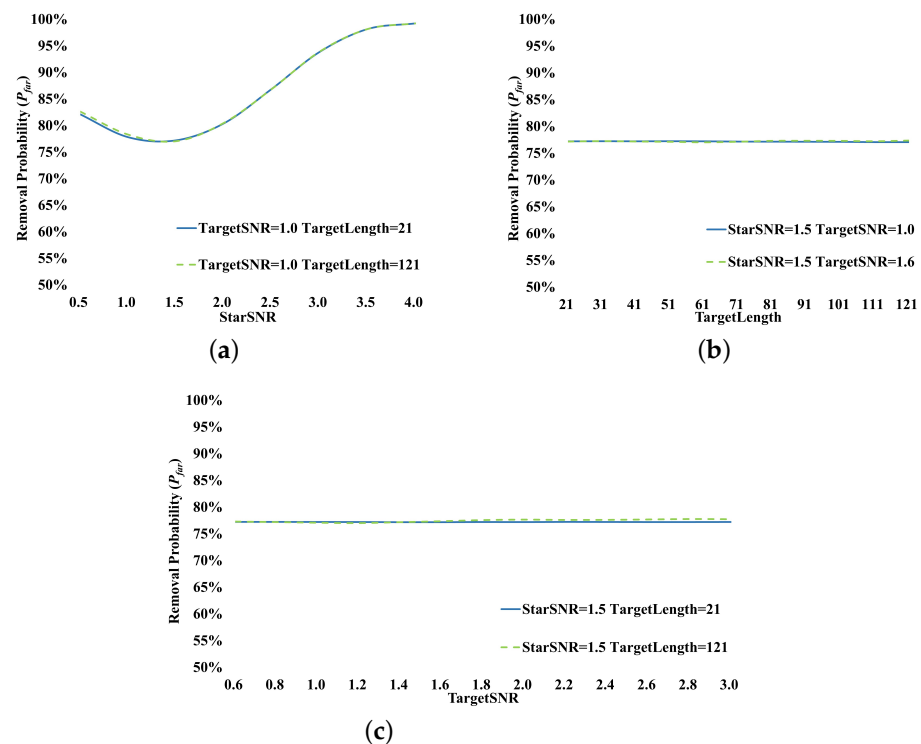


Figure 17. P_{far} of the perpendicular-cross filtering. (a) P_{far} with different star SNR; (b) P_{far} with different target lengths; (c) P_{far} with different target SNR.

Figure 18a shows that P_{ttr} is independent of the star SNR. Figure 18c shows that PCF has a significant negative impact on the detection of faint targets when the target SNR is less than 1.0. Because the filtering responses of very faint targets are largely dominated by noise, these targets may not meet the target requirements of PCF and so be deleted. Moreover, the number of true targets detected by matched filtering without PCF is also low in such a situation. When the target SNR exceeds 1.0, the P_{ttr} is greater than 98.5% and fluctuates slightly around 99% as the target length increases as illustrated in Figure 18b,c. This little negative impact on target detection is worthwhile and negligible compared to its

contribution to reducing false positives. When the target SNR exceeds 1.6, the P_{ttr} is almost 100% and is independent of the target length. Therefore, for targets with an SNR greater than 1.0, PCF can be well used to reduce false positives with little or even no negative impact on faint target detection.

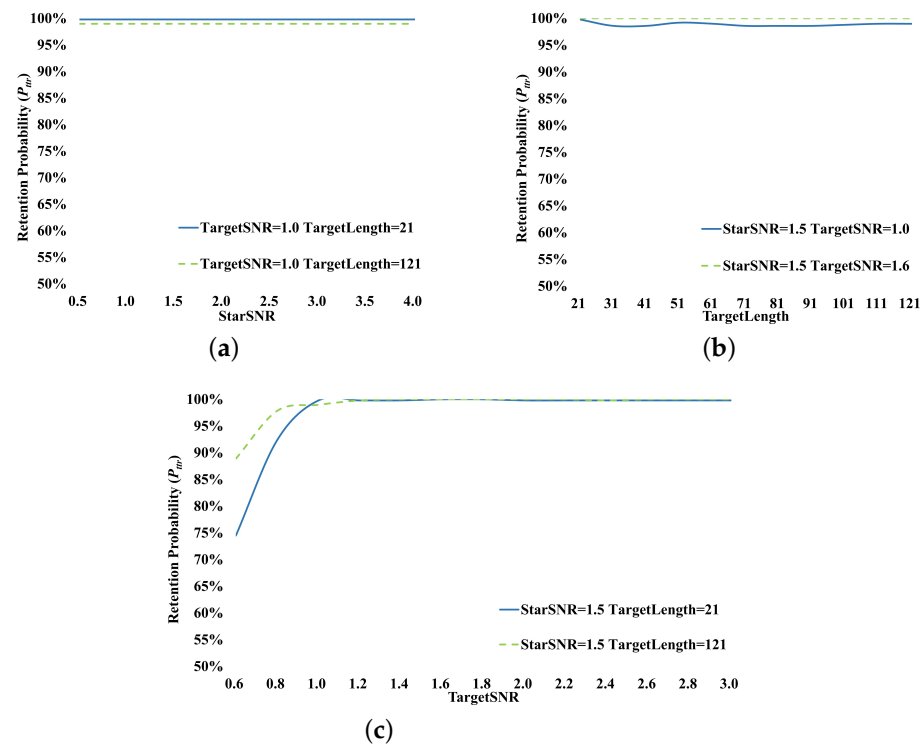


Figure 18. P_{ttr} of the perpendicular-cross filtering. (a) P_{ttr} with different star SNR; (b) P_{ttr} with different target lengths; (c) P_{ttr} with different target SNR.

5. Experiment and Discussion

As the characteristics of the simulated targets are precisely known, it was possible to draw exactly the figure of performance. Real star images were used to confirm the detection capability and reliability of the proposed method. The experimental environment was as follows: CPU is Intel Core i7-1355U (basic frequency 1.70 GHz and max turbo frequency 5.0 GHz), internal storage is 32 GB, and the program is coded in Matlab R2021a.

5.1. Simulated Star Images

The simulated star image is 1024×1024 in size and has 16-bit gray scales. The stray light in the star image is simulated by a powerful source at $[-50, -50]$. The background's mean and standard deviation are 6000 and 570, respectively. In the star image, 200 points of spike noise are randomly generated. Each star image includes 75 stars and 5 streak-like targets, with the star SNR ranging from 0.5 to 5 in steps of 0.5, the target SNR ranging from 0.6 to 5.0 in steps of 0.2, and the target length ranging from 21 pixels to 121 pixels in steps of 10 pixels. And the directions of five streak-like targets are -60° , -15° , 0° , 45° , and 90° , respectively. The baseline for comparison consists of the traditional threshold segmentation and the typical streak-like matched filtering, abbreviated as "TTS & SMF without PCF". The method proposed in this paper consists of dual-threshold segmentation, improved streak-like matched filtering, and perpendicular cross filtering, abbreviated as "DTS & ISMF with PCF". Target recognition probability (P_{tr}), false alarm probability (P_{fa}), and computational cost are used to evaluate the performance of the proposed method. The definitions of them are described in Section 4.3.

5.1.1. Target Recognition Probability

Figure 19 shows that the P_{tr} of the two methods is only related to the SNR and length of the target. The higher the target SNR, the greater the response of the matched filtering, and the lower the probability of the target being divided into multiple fragments; hence, the P_{tr} of the proposed method increases as the target SNR increases. As implemented and validated in Section 4.3, TTS cannot maintain the completeness of faint targets that may seriously deteriorate the P_{tr} , so the P_{tr} of the baseline method has a significant drop when the target SNR ranges from 1.0 to 2.4 in Figure 19b,c.

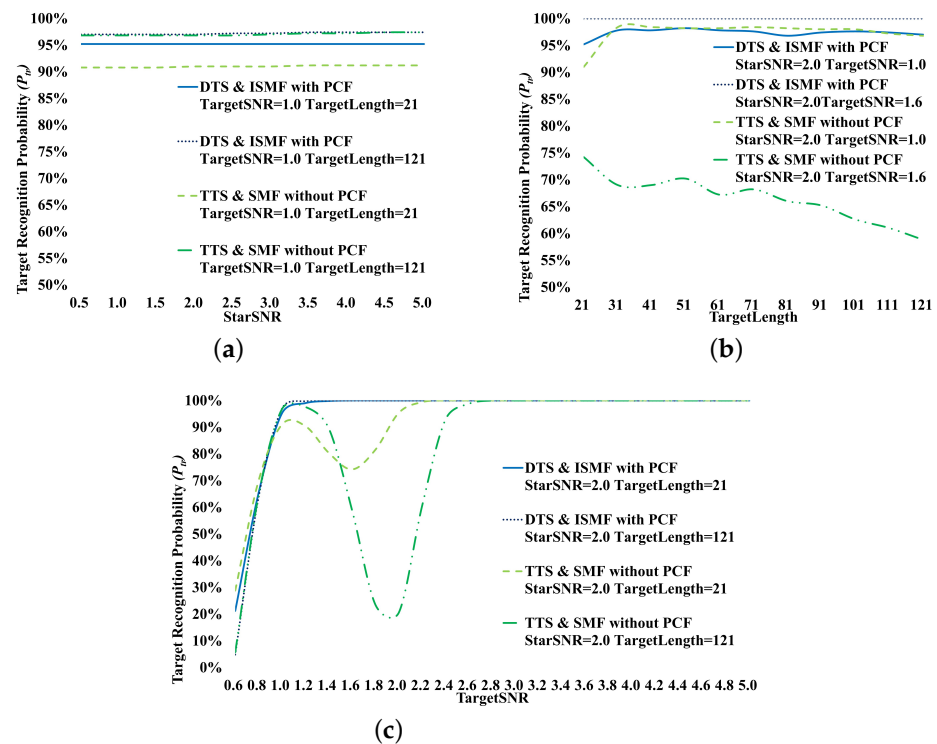


Figure 19. Comparison of experimental results on target recognition probability. (a) P_{tr} with different star SNR; (b) P_{tr} with different target lengths; (c) P_{tr} with different target SNR.

As shown in Figure 19b, when the target SNR is equal to 1.6, the P_{tr} of the proposed method is 100%, and it is not affected by the length of the target since the filtering response of the target can well meet the recognition requirements of matched filtering. When the target SNR is less than 1.6, the proposed method's P_{tr} for the 21-pixel length target is significantly lower than that of other length targets as shown in Figure 19a,b. As discussed in Section 3.2.1, when the target's length is close to that of the matched filtering unit, the filtering response is smaller than that of other length targets. For the baseline method, when the target SNR is equal to 1.6, the P_{tr} is severely damaged by TTS, and the longer the target length, the higher the probability of damage. Therefore, the P_{tr} of the baseline method will significantly deteriorate as the target length increases. When the target SNR is near 1.0 or more than 2.4, the P_{tr} is not significantly impacted by the target length because the target SNR is outside the range of the damage caused by TTS.

The baseline method severely deteriorates the detectability of faint targets since TTS may damage them. In contrast, the proposed method has a stable and good P_{tr} , allowing it to be applied to a wide range of SNR targets, whether bright or faint. Meanwhile, it can be seen that the P_{tr} of the proposed method can reach over 95% for targets with SNR greater than 1. When the SNR is greater than 1.2, the P_{tr} can reach over 99%. Therefore, the proposed method completely maintains the advantages of matched filtering in terms of high sensitivity and also provides a better environment for detecting faint targets.

5.1.2. False Alarm Probability

Figure 20 shows that P_{fa} is primarily impacted by the star SNR, and slightly changes as the target SNR or length changes. As mentioned in Section 3, the higher the SNR of stars in the dark layers, the more likely they are to be recognized as false positives, so P_{fa} increases as the star SNR increases. However, as the star SNR further increases, they will be separated into the bright layer, and the residual stars in the dark layers will decrease. Therefore, when the star SNR ranges from 1.5 to 2.0, the P_{fa} reaches its peak, then gradually declines before stabilizing as the star SNR increases as shown in Figure 20a.

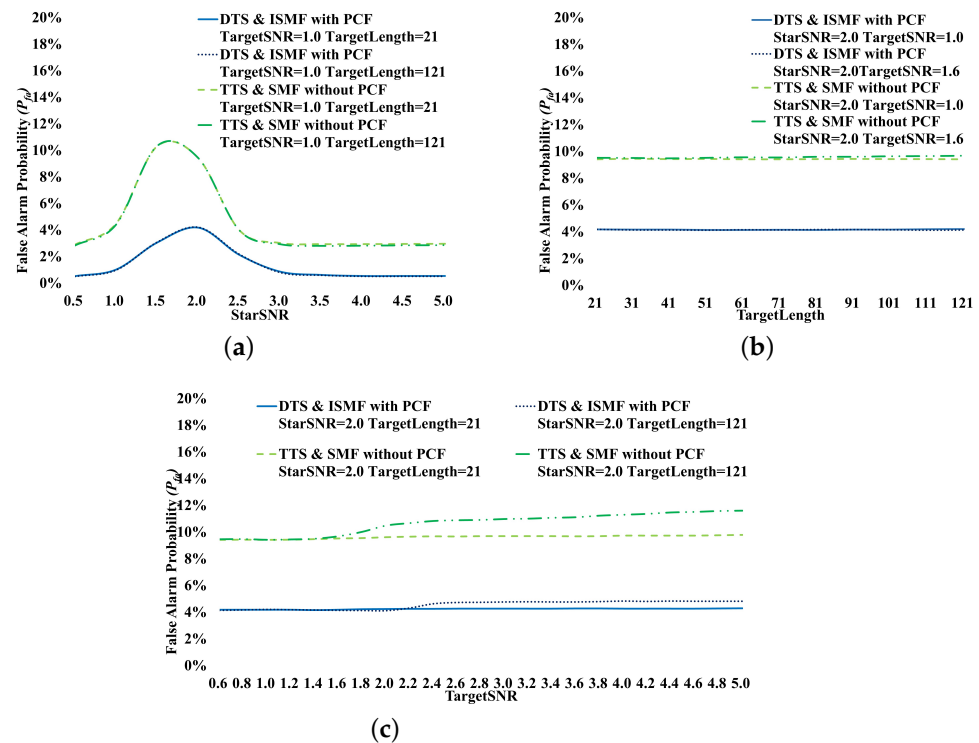


Figure 20. Comparison of experimental results on false alarm probability. (a) P_{fa} with different star SNR; (b) P_{fa} with different target lengths; (c) P_{fa} with different target SNR.

Figure 20a also shows that the P_{fa} of the proposed method is significantly better than that of the baseline method at different SNR. Figure 20c shows a sudden change in the P_{fa} of a streak-like target with a length of 121 pixels when the target SNR ranges from 1.6 to 2.4. According to Section 4.3, when the target SNR exceeds this range, most of the targets are segregated into bright layers, and these target areas are not counted in the noise statistics of the dark layer. While the target SNR falls below this range, these areas remain in the black layer and are counted in the noise statistics. As the statistical intensity of noise slightly decreases, the recognition threshold will also slightly decrease, resulting in more false positives. For streak-like targets with a length of 21 pixels, the change in the P_{fa} is not obvious because the target area is too small to have a little impact on noise statistics. This is also the reason why P_{fa} slightly changes with the length of the targets. From Figure 20b,c, it can also be seen that the P_{fa} of the proposed method is significantly better than that of the baseline method.

Residual stars and noise may be misidentified as targets due to the high susceptibility of matched filtering to interference. As shown in Figure 20, the P_{fa} of the baseline method can reach about 12%. However, the proposed method will eliminate a large number of false positives, lowering P_{fa} to less than 5% due to the use of PCF. Therefore, it can be concluded that the proposed method can effectively reduce false alarms in various situations.

5.1.3. Computational Cost

In order to evaluate the improvement effect of the proposed method in terms of computational cost, a serial execution program instead of the built-in function in Matlab is used to implement the matched filtering. The computational time for a single star image is calculated with 100 simulated star images to evaluate the improvement in computational complexity. The computational complexity of DTS is equivalent to twice that of TTS, and the proposed approach includes an additional PCF, which is also a type of matched filtering. However, the threshold segmentation requires a little calculation, and the computational complexity of a PCF, a specific filter, only relates to the potential target areas. These additional computations in the proposed method are negligible compared to the typical matched filtering. The experimental results in Table 2, which show a 74.75% decrease in computational cost, nearly equal to the 74.83% decrease in the matched filter in Section 4.4, demonstrate that the time cost of both methods is mainly dominated by matched filtering, and the proposed method has a significant computational cost advantage.

Table 2. Comparison of experimental results on computational cost.

	Baseline Method (TTS & SMF Without PCF)	Proposed Method (DTS & ISMF with PCF)
Consumption Time	408.765 s	103.197 s

5.2. Real Star Images

The real star image is provided by the Xi'an Institute of Optics and Precision Mechanics specifically for faint target recognition as shown in Figure 21. The size of the real star image is 1024×1024 , and its grayscale level is 16 bits. There are two faint streak-like targets in the image, shown by the blue square in Figure 21. The endpoints of the first target are located approximately at (417,477) and (411,507). Its length is approximately 32 pixels, and its direction is approximately 13° . The other target's endpoints are located approximately at (900,768) and (858,780). Its length and direction are approximately 45 pixels and 73° , respectively.

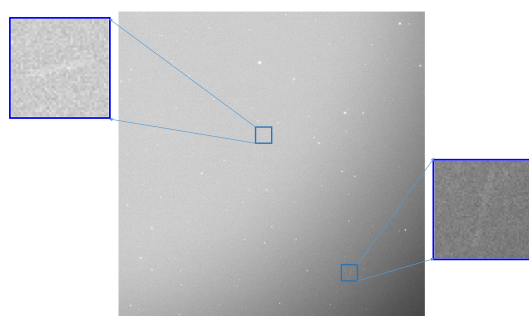


Figure 21. Raw real star image.

Both processes of the baseline and proposed methods are shown in Figure 22. The saturated layer, background estimation, and spike noise are shown in Figure 22a–c, respectively. The result of the baseline method has one more bright object represented by the blue square than the improved method as shown in Figure 22d,g. Because this bright object is a space target and its intensity is near the segmentation threshold, it is destructively split and incorrectly detected as a star in the bright layer and a space target in the dark layer using the baseline method. However, the same target is completely separated and correctly detected in the dark layer using the improved method as shown in Figure 22g,h. The results demonstrate that the improved method has the advantage of maintaining the completeness of faint targets. The detected objects in the dark layer are shown by the yellow-dot rectangle

in Figure 22e,h. It can be found that the problem of false positives caused by residual stars and noise is serious in the dark layer using the baseline method. The proposed method can effectively reduce false positives in the dark layer.

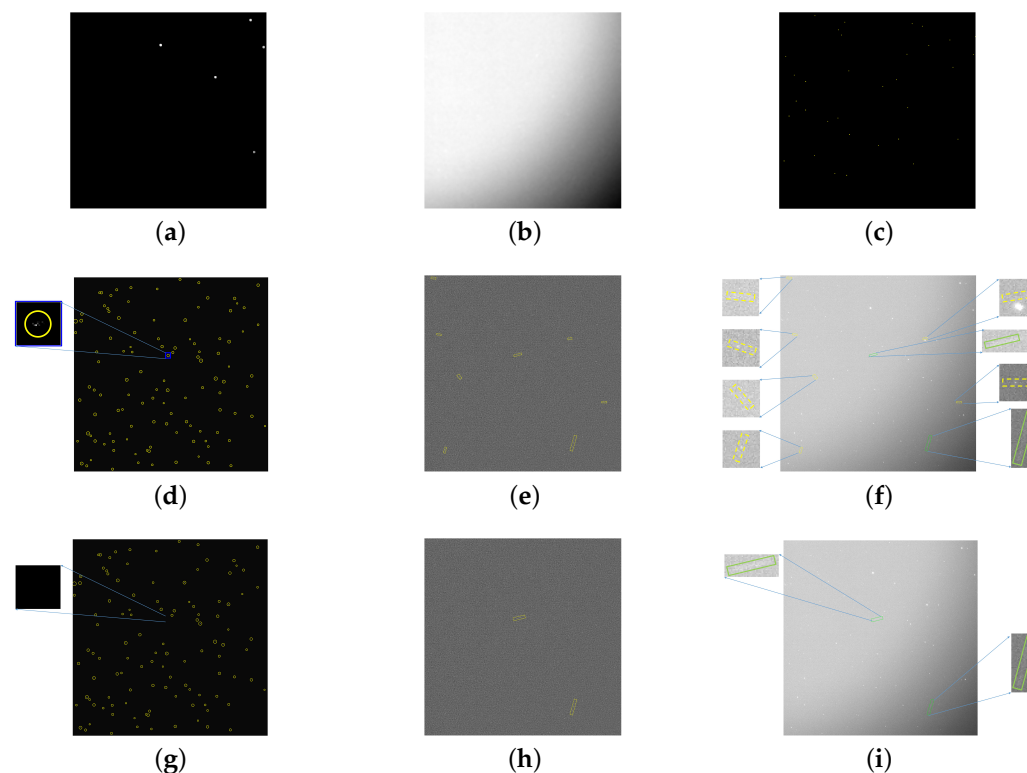


Figure 22. The detection results of the real star image by the baseline and proposed methods. (a) saturated layer. (b) Background estimation. (c) Spike noise. (d) Bright layer by the baseline method. (e) Dark layer by the baseline method. (f) Detection results by the baseline method. (g) Bright layer by the proposed method. (h) Dark layer by the proposed method. (i) Detection results by the proposed method.

Because there are no targets in the bright layer, the identified targets in the dark layer determine the final results in the real star image. Figure 22f shows the results of the baseline method, which detects not only the two targets shown by the green-line rectangle but also six false positives shown by the yellow-dot rectangle. In contrast, the proposed method successfully detects two targets shown by the green-line rectangle with no false positives as shown in Figure 22i. It can be seen that the proposed method maintains the high detection sensitivity of typical matched filtering while effectively filtering out false positives. Therefore, it is concluded that the method proposed in this study is superior to the baseline method, and it can be successfully used for detecting multiple faint streak-like targets in a single real star image.

6. Conclusions

This study presented an improved method for detecting multiple faint targets in a single star image. The central concept of the method is matched filtering, which can integrate all the distributed energy of streak-like targets to improve the detection sensitivity. However, matched filtering is computationally intensive and prone to producing false positives. The proposed method includes three improved approaches conducted in three stages of matched filtering to address these issues. Firstly, image layering is performed before matched filtering, which involves identifying and removing saturated and bright targets. Using TTS to separate bright layers can damage targets, resulting in the targets

being missed or identified as stars. DTS can reduce the target damage probability from 90% to within 1%, compared with TTS. Secondly, reducing the complex calculations in matched filtering is very important. The use of the streak-like matched filter unit and the dual-step search can reduce the computational cost to within 1/4 that of traditional matched filtering. Finally, false positives are eliminated through the use of the PCF after matched filtering. The false alarm probability can be improved by 77%, while the negative impact on the accuracy of target detection does not exceed 1.5%.

Experiments with simulated and real star images were conducted to test the end-to-end performance of the improved method. When the target SNR was greater than 1.2, the target recognition probability reached over 99%, and the false alarm probability was less than 5% in the experiments using simulated star images. In the experiments using real star images, both faint targets in a single star image were correctly detected without any false positives. These experiments demonstrated that the proposed method has significant advantages for detecting multiple faint targets in a single star image. In conclusion, the proposed method enables enhanced target detection through improving the detection environment, simplifying the matched filtering process, and removing false positives, resulting in high detection accuracy, reasonable computational cost, and fewer false alarms. This method is not only suitable for detecting multiple targets in a single star image but it also has reference significance in the context of star image compression, star image registration, and target characteristic extraction.

Author Contributions: Conceptualization, Y.H. and D.W.; methodology, Y.H. and D.W.; software, Y.H. and Z.Q.; validation, Y.H., J.L. and Z.Q.; formal analysis, Y.H.; investigation, Y.H.; resources, Y.H. and D.W.; data curation, Y.H. and Z.Q.; writing—original draft preparation, Y.H.; writing—review and editing, Y.H., D.W., J.L. and Z.Q.; visualization, Y.H.; supervision, D.W. and J.L.; project administration, D.W.; funding acquisition, D.W. and J.L. All authors have read and agreed to the published version of the manuscript.

Funding: This research received no external funding.

Data Availability Statement: Data underlying the results presented in this paper are not publicly available at this time but may be obtained from the authors upon reasonable request.

Conflicts of Interest: The authors declare no conflicts of interest.

References

1. Svtina, V.; Cherkasova, M. Space debris removal—Review of technologies and techniques. Flexible or virtual connection between space debris and service spacecraft. *Acta Astronaut.* **2023**, *204*, 840–853. [[CrossRef](#)]
2. Miraux, L. Environmental limits to the space sector's growth. *Sci. Total Environ.* **2022**, *806*, 150862. [[CrossRef](#)] [[PubMed](#)]
3. Li, B.; Huang, J.; Feng, Y.; Wang, F.; Sang, J. A machine learning-based approach for improved orbit predictions of LEO space debris with sparse tracking data from a single station. *IEEE Trans. Aerosp. Electron. Syst.* **2020**, *56*, 4253–4268. [[CrossRef](#)]
4. Tao, J.; Cao, Y.; Ding, M. Progress of space debris detection technology. *Laser Optoelectron. Prog.* **2022**, *59*, 1415010.
5. Hu, Y.; Li, K.; Liang, Y.; Chen, L. Review on strategies of space-based optical space situational awareness. *J. Syst. Eng. Electron.* **2021**, *32*, 1152–1166.
6. Han, Y.; Wen, D.; Li, J. Fast registration method for sequential star images. *Appl. Opt.* **2023**, *62*, 7316–7329. [[CrossRef](#)]
7. Lin, B.; Yang, X.; Wang, J.; Wang, Y.; Wang, K.; Zhang, X. A robust space target detection algorithm based on target characteristics. *IEEE Geosci. Remote Sens. Lett.* **2021**, *19*, 8012405. [[CrossRef](#)]
8. He, Y.; Wang, H.; Feng, L.; You, S. A novel method of eliminating stray light interference for star sensor. *IEEE Sens. J.* **2020**, *20*, 8586–8596. [[CrossRef](#)]
9. Do, H.; Chin, T.; Moretti, N.; Jah, M.K.; Tetlow, M. Robust foreground segmentation and image registration for optical detection of GEO objects. *Adv. Space Res.* **2019**, *64*, 733–746. [[CrossRef](#)]
10. Su, S.; Niu, W.; Li, Y.; Ren, C.; Peng, X.; Zheng, W.; Yang, Z. Dim and small space-target detection and centroid positioning based on motion feature learning. *Remote Sens.* **2023**, *15*, 2455. [[CrossRef](#)]

11. Sun, Q.; Niu, Z.; Wang, W.; Li, H.; Luo, L.; Lin, X. An adaptive real-time detection algorithm for dim and small photoelectric GSO debris. *Sensors* **2019**, *19*, 4026. [[CrossRef](#)] [[PubMed](#)]
12. Torteeka, P.; Gao, P.; Shen, M.; Guo, X.; Yang, D.; Yu, H.; Zhou, W.; Tong, L.; Zhao, Y. Autonomous space target tracking through state estimation techniques via ground-based passive optical telescope. *Adv. Space Res.* **2019**, *63*, 461–475. [[CrossRef](#)]
13. Du, J.; Hu, S.; Chen, X.; Cao, H.; Jiang, Y. Simulating photometric images of moving targets with photon-mapping. *Publ. Astron. Soc. Pac.* **2021**, *133*, 104501. [[CrossRef](#)]
14. Vere, P.; Jedicke, R.; Denneau, L.; Wainscoat, R.; Holman, M.J.; Lin, H.W. Improved asteroid astrometry and photometry with trail fitting. *Publ. Astron. Soc. Pac.* **2012**, *124*, 1197. [[CrossRef](#)]
15. Wan, X.; Wang, G.; Wei, X.; Li, J.; Zhang, G. ODCC: A dynamic star spots extraction method for star sensors. *IEEE Trans. Instrum. Meas.* **2021**, *70*, 5009114. [[CrossRef](#)]
16. Virtanen, J.; Poikonen, J.; Säntti, T.; Komulainen, T.; Torppa, J.; Granvik, M.; Muinonen, K.; Pentikäinen, H.; Martikainen, J.; Näränen, J.; et al. Streak detection and analysis pipeline for space-debris optical images. *Adv. Space Res.* **2016**, *57*, 1607–1623. [[CrossRef](#)]
17. Dawson, W.A.; Schneider, M.D.; Kamath, C. Blind detection of ultra-faint streaks with a maximum likelihood method. *arXiv* **2016**, arXiv:1609.07158.
18. Leu, J.G. A computer vision process to detect and track space debris using ground-based optical telephoto images. In Proceedings of the 1992 11th IAPR International Conference on Pattern Recognition, The Hague, The Netherlands, 30 August–3 September 1992; Volume 1, pp. 522–525.
19. Schildknecht, T.; Hugentobler, U.; Verdun, A. Algorithms for ground based optical detection of space debris in GEO and GTO. In Proceedings of the 1st International Workshop on Space Debris, Moscow, Russia, October 1995; pp. 47–50.
20. Harrison, D.C.; Chow, J.C. The space-based visible sensor. *Johns Hopkins APL Tech. Dig.* **1996**, *17*, 227.
21. Gural, P.S.; Larsen, J.A.; Gleason, A.E. Matched filter processing for asteroid detection. *Astron. J.* **2005**, *130*, 1951. [[CrossRef](#)]
22. Yanagisawa, T.; Nakajima, A.; Kadota, K.; Kurosaki, H.; Nakamura, T.; Yoshida, F.; Dermawan, B.; Sato, Y. Automatic detection algorithm for small moving objects. *Publ. Astron. Soc. Jpn.* **2005**, *57*, 399–408. [[CrossRef](#)]
23. Danescu, R.G.; Itu, R.; Muresan, M.P.; Rednic, A.; Turcu, V. SST Anywhere—A Portable Solution for Wide Field Low Earth Orbit Surveillance. *Remote Sens.* **2022**, *14*, 1905. [[CrossRef](#)]
24. Zhang, B.; Hu, S.; Du, J.; Yang, X.; Chen, X.; Jiang, H.; Cao, H.; Feng, S. Detecting Moving Objects in Photometric Images Using 3D Hough Transform. *Publ. Astron. Soc. Pac.* **2024**, *136*, 054502. [[CrossRef](#)]
25. Stoveken, E.; Schildknecht, T. Algorithms for the optical detection of space debris objects. In Proceedings of the 4th European Conference on Space Debris, Darmstadt, Germany, 18–20 April 2005; pp. 18–20.
26. Koupryanov, V. Distinguishing features of CCD astrometry of faint GEO objects. *Adv. Space Res.* **2008**, *41*, 1029–1038. [[CrossRef](#)]
27. Lin, B.; Zhong, L.; Zhuge, S.; Yang, X.; Yang, Y.; Wang, K.; Zhang, X. A New Pattern for Detection of Streak-Like Space Target From Single Optical Images. *IEEE Trans. Geosci. Remote Sens.* **2021**, *60*, 5616113. [[CrossRef](#)]
28. Yanagisawa, T.; Nakajima, A. Detection of small LEO debris with line detection method. *Trans. Jpn. Soc. Aeronaut. Space Sci.* **2005**, *47*, 240–248. [[CrossRef](#)]
29. Zimmer, P.C.; Ackermann, M.R.; McGraw, J.T. GPU-accelerated faint streak detection for uncued surveillance of LEO. In Proceedings of the 2013 AMOS Technical Conference, Maui, HI, USA, 10–13 September 2013; p. 31.
30. Hickson, P. A fast algorithm for the detection of faint orbital debris tracks in optical images. *Adv. Space Res.* **2018**, *62*, 3078–3085. [[CrossRef](#)]
31. Ciurte, A.; Danescu, R. Automatic detection of meo satellite streaks from single long exposure astronomic images. In Proceedings of the 2014 International Conference on Computer Vision Theory and Applications (VISAPP), Lisbon, Portugal, 5–8 January 2014; Volume 1, pp. 538–544.
32. Tagawa, M.; Yanagisawa, T.; Kurosaki, H.; Oda, H.; Hanada, T. Orbital objects detection algorithm using faint streaks. *Adv. Space Res.* **2016**, *57*, 929–937. [[CrossRef](#)]
33. Nir, G.; Zackay, B.; Ofek, E.O. Optimal and efficient streak detection in astronomical images. *Astron. J.* **2018**, *156*, 229. [[CrossRef](#)]
34. Levesque, M.P.; Buteau, S. *Image Processing Technique for Automatic Detection of Satellite Streaks*; Defense Research and Development Canada: Valcartier, QC, Canada, 2007.
35. Lvesque, M.; Lelièvre, M. *Improving Satellite-Streak Detection by the Use of False Alarm Rejection Algorithms*; DRDC Valcartier TR 2006-587; Defense Research and Development Canada: Valcartier, QC, Canada, 2011.
36. Vananti, A.; Schild, K.; Schildknecht, T. Streak detection algorithm for space debris detection on optical images. In Proceedings of the AMOS Conference, Maui, HI, USA, 15–18 September 2015; p. 262.
37. Vananti, A.; Schild, K.; Schildknecht, T. Improved detection of faint streaks based on a streak-like spatial filter. *Adv. Space Res.* **2020**, *65*, 364–378. [[CrossRef](#)]
38. Guo, X.; Chen, T.; Liu, J.; Liu, Y.; An, Q. Dim space target detection via convolutional neural network in single optical image. *IEEE Access* **2022**, *10*, 52306–52318. [[CrossRef](#)]

39. Zhao, H.; Sun, R.Y.; Yu, S.X. Deep Neural Network Closed-loop with Raw Data for Optical Resident Space Object Detection. *Res. Astron. Astrophys.* **2024**, *24*, 115009. [[CrossRef](#)]
40. Guo, Y.; Yin, X.; Xiao, Y.; Zhao, Z.; Yang, X.; Dai, C. Enhanced YOLOv8-based method for space debris detection using cross-scale feature fusion. *Discov. Appl. Sci.* **2025**, *7*, 95. [[CrossRef](#)]
41. Levesque, M. Automatic reacquisition of satellite positions by detecting their expected streaks in astronomical images. In Proceedings of the Advanced Maui Optical and Space Surveillance Technologies Conference, Maui, HI, USA, 1–4 September 2009; p. E81.
42. Xi, J.; Wen, D.; Ersoy, O.K.; Yi, H.; Yao, D.; Song, Z.; Xi, S. Space debris detection in optical image sequences. *Appl. Opt.* **2016**, *55*, 7929–7940. [[CrossRef](#)] [[PubMed](#)]

Disclaimer/Publisher’s Note: The statements, opinions and data contained in all publications are solely those of the individual author(s) and contributor(s) and not of MDPI and/or the editor(s). MDPI and/or the editor(s) disclaim responsibility for any injury to people or property resulting from any ideas, methods, instructions or products referred to in the content.